

Investigation of an overlap of heating peaks in the hypersonic boundary layer over a blunt cone

Zhenghao Feng , Chong Cai, and Cunbiao Lee ^{*}

State Key Laboratory of Turbulence and Complex Systems, *Peking University*, Beijing 100871, China

Daoning Yang

Space Engineering University, Beijing 101416, China



(Received 29 December 2023; accepted 5 June 2024; published 1 July 2024)

An overlap of two heating peaks in a Mach 6 hypersonic boundary layer over a flared cone with a small nose bluntness at a freestream Reynolds number of $10.0 \times 10^6 \text{ m}^{-1}$ is experimentally observed. It is found that a small bluntness can only delay the evolution of the second mode, which reduces but does not eliminate the dilatation-induced heating peak before the shear-induced heating peak. The approach of the saturation location of the second mode and the onset location of transition indicated by the broadening disturbance spectrum leads to shorter hot streaks and low-temperature valleys over the blunt cone. The simulations using the random forcing replicate the measured instability spectra qualitatively. A heating decomposition is conducted to confirm that the initial peak over both cones is due to the second mode.

DOI: [10.1103/PhysRevFluids.9.L071901](https://doi.org/10.1103/PhysRevFluids.9.L071901)

Introduction. Laminar-turbulent transition in boundary layers has a crucial effect on the aerodynamic heating and surface skin friction of vehicles at hypersonic speeds, the neglect of which will pose great threats to flight safety [1–3]. Since many high-speed vehicles have blunt noses, recent decades have seen a rapid growth of research on nose bluntness effects on the hypersonic boundary layer transition. Early laminar stability measurements over Mach 8 sharp and blunt cones have been thoroughly documented by Stetson *et al.* [4–6]. Compared with a sharp cone, the presence of the bow shock and resultant entropy layer [7] over a blunt cone greatly reduces the receptivity to freestream acoustic waves [8–11] and stabilizes the boundary layer when the nose bluntness is small [5,10,12–15]. The location at which the second mode begins to amplify is directly associated with the entropy swallow point [16,17]. A phenomenon of transition reversal was observed in early experiments in the case of large nose bluntness [18,19], and its verification and explanation has become a key topic [14,20–22]. Many studies have reported an extra heating peak before the onset of hypersonic transition on a sharp flared cone [23–27], and the direct relationship between this peak and the high-frequency compression and expansion of fluid accompanying the second mode has been identified [26,27]. The previous work focused on the influence of nose bluntness on flow stability, but the instability-related aerodynamic heating has rarely been investigated.

In this Letter, we report an experimental observation of an overlap of two heating peaks in a Mach 6 boundary layer over a flared cone with a small nose bluntness. Instability measurements and heating decomposition are conducted to explain this intriguing phenomenon.

Experimental setup. The experiments were conducted in a Mach 6 hypersonic quiet wind tunnel (M6QT) at Peking University [27–29], the performance of which gained widespread recognition

^{*}Contact author: cblee@mech.pku.edu.cn

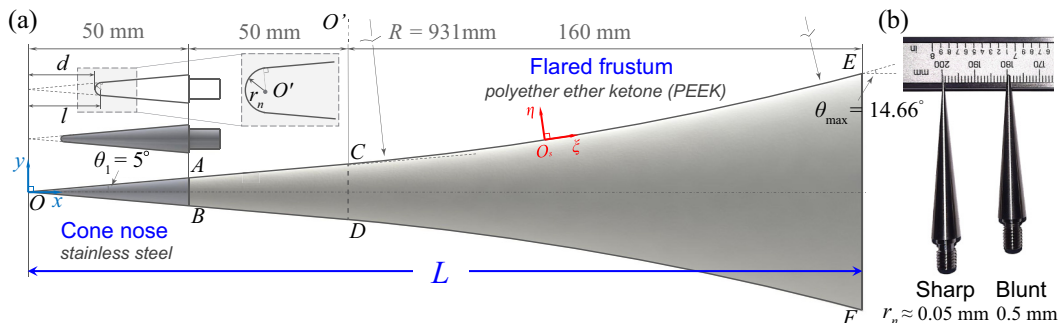


FIG. 1. (a) Schematic of model with noses of different tip radius. (b) Photograph of the noses.

[30,31]. To promote instability waves and trigger early transition, the noisy condition was used, and the normalized pitot pressure fluctuations p'_0/p_0 was about 2.20% [32]. The flow was preheated upstream to avoid liquification in the test section.

The base model shown in Fig. 1 is a 260 mm long, flared, instability-enhanced cone with interchangeable noses [28,33]. The radius is approximately 0.05 mm for the sharp tip ($Re_{r_{nose}} = 500$) which meets the “sharp” criterion used at NASA Langley ($Re_{r_{nose}} < 1000$, [34]) for the sharp tip after the finish machining, and 0.5 mm for the blunt tip. The entropy swallowing distance on the sharp cone is below 10 mm according to the base flow calculation. The frustum is made of polyether ether ketone (PEEK) with high emissivity. The cone was first manually calibrated to zero angle of attack using a gradiometer. Fine adjustment is then applied through test runs to ensure the up-down symmetry of the measured results.

The real-time surface temperature distribution, which reflects the intensity of time-integrated heating, was measured by infrared (IR) thermography [35]. A long-wave infrared camera was used, which has a sensitive temperature range from -40 to $+650$ °C, a thermal sensitivity below 0.04 K, a frequency of 30 Hz, and a spectral range of 7.5 to 14 μm . The recording lasts for 20 s to capture the whole heating procedure.

Focused laser differential interferometry (FLDI), an advanced experimental technique featuring a noncontact optical setup, was applied to measure the disturbance development in the boundary layer [29,36,37]. FLDI can capture MHz disturbances sensitive to the density gradient in a small region near the focused point. The multiple-point measurements were performed. For a targeted streamwise location, the beam was initially lifted to a certain height with steps of 0.05 mm (regarded as the wall) where it was just not obscured by the model indicated by a jump in received signals. Then, the beam was lifted vertically across the boundary layer for 1.5 mm at intervals of 0.1 mm. The power spectral densities (PSDs) of disturbances filtered in a passband of [5, 1000] kHz were obtained by Welch’s method [38].

Numerical setup. To support the experiments, three-dimensional (3-D) direct numerical simulations (DNS) were conducted using OpenCFD software [39]. The simulations used an axisymmetric mesh of 3000 (streamwise) \times 180 (wall normal) \times 120 (circumferential) for the sharp cone and 3700 \times 188 \times 120 for the blunt cone, covering an azimuthal range of $\varphi = [-\pi/16, \pi/16]$ with the maximum $\Delta y_w^+ \approx 1.0$ where the subscript “w” represents wall. A strategy was adopted to adapt grids to the outline of the bow shock over the blunt cone to improve resolution, inspired by a hypersonic receptivity study [40]. The boundary and initial conditions were the same as those in [27], except for the excitation of disturbances. A random forcing approach was adopted to simulate the “natural” transition [41]. The forcing region for both cones was near the 3-D inflow boundary from the wall to the boundary-layer edge covering the entire spanwise domain. A pseudorandom number generator was employed to apply 3% pressure and 3% velocity perturbances at intervals of time steps to make the saturation location of the second mode on the sharp cone close to the measurement. The conditions were the same as those in the experiments, corresponding to a

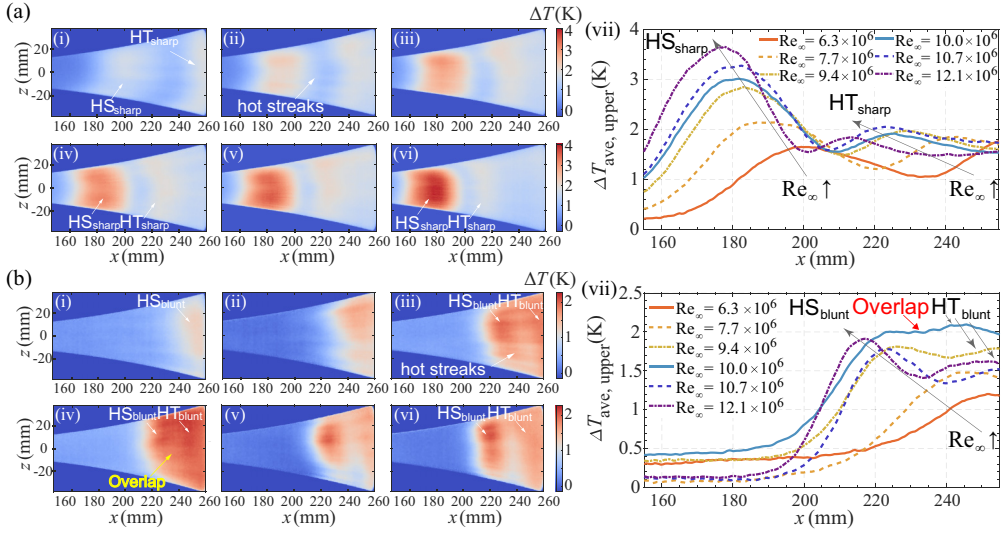


FIG. 2. Contours of wall temperature rise for 4 s on (a) the sharp cone and (b) the blunt cone: (i) $Re_\infty = 6.3 \times 10^6 \text{ m}^{-1}$; (ii) $7.7 \times 10^6 \text{ m}^{-1}$; (iii) $9.4 \times 10^6 \text{ m}^{-1}$; (iv) $10.0 \times 10^6 \text{ m}^{-1}$; (v) $10.7 \times 10^6 \text{ m}^{-1}$; (vi) $12.1 \times 10^6 \text{ m}^{-1}$; (vii) plots of the spanwise-averaged ΔT obtained from the upper half contour.

stagnation pressure $p_0 = 0.88 \times 10^6 \text{ Pa}$, a stagnation temperature $T_0 = 415 \text{ K}$, and a freestream Reynolds number $Re_\infty = 10.0 \times 10^6 \text{ m}^{-1}$. For the partitioning, meshes, numerical methods, and details of forcing, see the Supplemental Material [42].

Results and discussion. Figure 2 shows the contours of wall temperature rise ΔT measured by the IR thermography during 4 s after the tunnel flow became steady at different Re_∞ . The contours are not full symmetric, especially for the blunt cone, due to the inhomogeneous freestream disturbances as well as the roughness effect of the sealed holes reserved for pressure transducers behind the lower side of the model. Thus, the variable $\Delta T_{\text{ave, upper}}$ representing the spanwise-averaged ΔT obtained from the upper half contour instead of the whole plane is plotted along the streamwise position. Two heating peaks can be clearly observed on the sharp cone for all values of Re_∞ , denoted as HS_{sharp} and HT_{sharp} , respectively. Herein, HS denotes the additional peak in heat transfer within the transitional region, while HT denotes a second rapid growth of heating near the end of transition that was confirmed by Rayleigh-scattering visualization [28,32]. The added subscript represents the sharp or blunt cone. As shown in Fig. 2(a)(vii), the strength of HS_{sharp} is increased with Re_∞ while that of HT_{sharp} changes little. Furthermore, multiple hot streaks stretching from the middle of HS_{sharp} to the front of HT_{sharp} are observable, similar to those in the experiments [23,25,48] and DNS [49,50]. The generation process of unsteady hot streaks in our random forcing DNS is shown in Fig. 3. Each streamwise streak is composed of amplified 3D waves featured with overlapped temperature peaks and with second-mode frequency. The valleys among pairs of neighboring waves become indistinct due to high wave amplitudes, which resembles the scenario suggested in [51] (see their Figs. 11 and 22) for incompressible flows.

For the blunt cone, however, the situation is more complex. For relatively low Re_∞ of 6.3×10^6 and $7.7 \times 10^6 \text{ m}^{-1}$, there is only one heating peak at the rear of the model. For relatively high Re_∞ of 10.7×10^6 and $12.1 \times 10^6 \text{ m}^{-1}$, two peaks with a gap near $x = 240 \text{ mm}$ are observed, denoted by HS_{blunt} and HT_{blunt} , just as in the sharp case. Thus, the only peak for two low- Re_∞ cases is actually HS_{blunt} . For moderate Re_∞ of 9.4×10^6 and $10.0 \times 10^6 \text{ m}^{-1}$, careful examination confirms the presence of two heating peaks. The two peaks can be distinguished by the uniformity of heating, with the former exhibiting uneven streaks and the latter being smoother. In addition, they

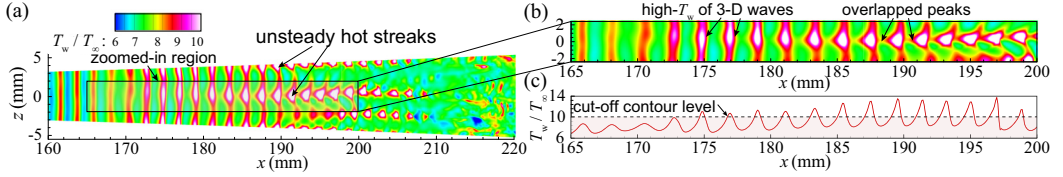


FIG. 3. Instantaneous calculated temperature on the adiabatic wall of sharp cone at $t = 0.257$ ms: (a) visualization of unsteady hot streaks; (b) zoomed-in region along a streak; (c) the plot of wall temperature along $z = 0$ mm, where the dash line indicates the cut-off contour level.

appear to overlap for a certain length, since the low-temperature gap is less obvious than that in two higher- Re_∞ cases.

The streamwise evolution of disturbance spectra at three wall-normal positions is compared in Fig. 4 to show the general variation of disturbance intensity in the boundary layer. Re_∞ was $10.0 \times 10^6 \text{ m}^{-1}$ corresponding to the case where the overlap of peaks is obvious. For both cones, the frequency peaks of the second mode near $f = 400$ kHz and its harmonics, as well as those of the low-frequency waves near $f = 15$ kHz, can be identified. The measured spectra evolved on the wall are similar to those in previous experiments obtained by pressure transducers [28,32]. The peaks become more prominent at the wall-normal height $\eta = 0.5$ mm and become less obvious at $\eta = 1.0$ mm near the edge of boundary layer. They are not created by the filter due to their broad ranges beyond the cut-off frequency of 5 kHz.

For the sharp cone, the second mode grows until $x = 175$ mm, and gradually decays before the disappearance of characteristic peak at $x = 205$ mm. According to the linear stability analysis [52], the characteristics of Görtler mode brought by the wall curvature are similar to those of the first mode, e.g., they are both shear-related modes travelling near the boundary layer edge with highly overlapped frequency ranges, which make them difficult to be distinguished only from the measured spectra. Thus, here the evolution of low-frequency components is examined as a whole. The low-frequency waves grow continuously before $x = 215$ mm, and the subsequent drop of its characteristic peak along with the broadening of disturbance spectrum indicates the onset of transition [6].

For the blunt cone, however, it is not until $x = 180$ mm that the second-mode peak appears. The second mode reaches its maximum near $x = 220$ mm and decays quickly. The low-frequency waves

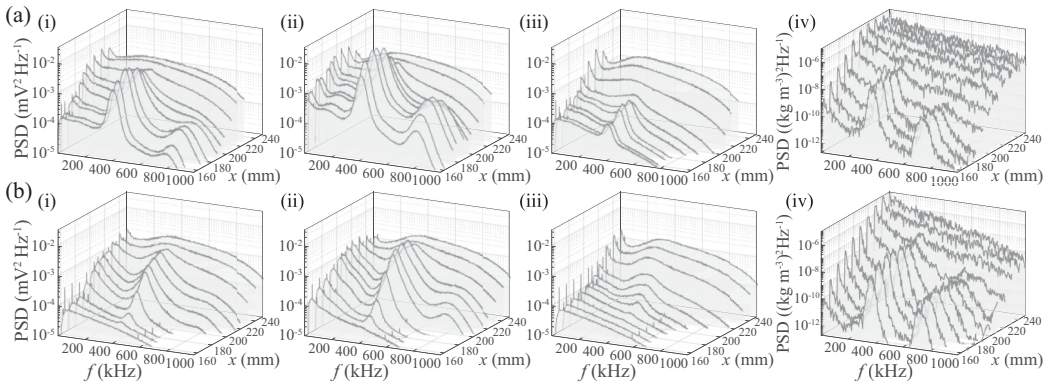


FIG. 4. Spatial evolution of PSDs on (a) the sharp cone and (b) the blunt cone: FLDI results (voltage signal) at (i) $\eta = 0.0 (\pm 0.05)$ mm; (ii) $\eta = 0.5 (\pm 0.05)$ mm; (iii) $\eta = 1.0 (\pm 0.05)$ mm; DNS results (density fluctuations) at (iv) $\eta = 0.5$ mm. $\text{Re}_\infty = 10.0 \times 10^6 \text{ m}^{-1}$.

keep growing before the broadening of spectrum at $x = 240$ mm. Therefore, the evolution of the second mode is significantly delayed. In addition, the trend of DNS spectra at $\eta = 0.5$ mm agrees well with the measurements.

The relationship between the instability evolution and heating peaks needs to be clarified. Considering the frequency shift and spatial displacement of the evolved waves, we define the local amplitude of an instability wave based on its statistic property at the position x as

$$M_{x, (f_1, f_2)} = \max_{\eta} \{M_{(x, \eta), (f_1, f_2)}\}, \quad 0.0 \text{ mm} \leq \eta \leq 1.5 \text{ mm}, \quad (1)$$

where $M_{(x, \eta), (f_1, f_2)}$ represents the root mean square of filtered time series at the point (x, η) with the passband (f_1, f_2) . The amplitude is then normalized by its streamwise maximum to obtain M_{norm} . The saturation location of each mode is defined as where the maximum M_{norm} appears. According to Fig. 4, the frequency ranges for FLDI spectra are set to be $(f_1, f_2) = (10, 30)$ and $(400, 420)$ kHz for the low-frequency waves and the second mode, respectively. The counterparts for DNS spectra are $(10, 30)$ and $(355, 375)$ kHz. The development of normalized amplitudes of two instability waves is presented in Fig. 5, plotted with an uncertainty of 5% estimated from repetitive measurements. The FLDI results show that, for the sharp cone, the saturation location of the second mode is a little upstream of the first heating peak HS_{sharp} and matches its gradient peak at $x = 170$ mm well. This can be explained by the following linearized energy equation for the two-dimensional steady flow:

$$\rho c_v U \frac{\partial T}{\partial x} = k \frac{\partial^2 T}{\partial \eta^2} + \phi(x, \eta), \quad (2)$$

where ρ , c_v , U , T , k are the density, specific heat, mean velocity, temperature, and thermal conductivity of the gas, and ϕ denotes the heat sources of pressure dilatation and viscous dissipation. The wall temperature $T_w(x)$ can be solved by Eq. (2) with a separate method [27]. It showed that ϕ dominates $(\partial T_w / \partial x)$ in the presence of highly amplified second mode, indicating the second-mode peak corresponds with the maximum wall temperature gradient. Furthermore, the second heating peak HT_{sharp} is located at $x = 225$ mm where the amplitude of the low-frequency waves decreases rapidly, which implies the near completion of transition.

For the blunt cone, two gradient peaks can be seen slightly upstream of HS_{blunt} and HT_{blunt} . Compared to the sharp cone, the saturation of the second mode is much delayed. In light of the shrunken distance between the saturation locations of the second mode and the low-frequency waves, and the downstream shift of HS_{blunt} relative to the second-mode peak, the former heating peak is more likely to approach the latter one. DNS results are also shown in Fig. 5. $\Delta T_{\text{cal}, w}$ represents the calculated dimensionless wall temperature relative to its base flow value. For both cones, the first temperature gradient peak matches the second-mode amplitude peak, which agrees well with the observation. The rapid increase of skin friction coefficient C_f (defined as $2\tau_w / \rho_{\infty} U_{\infty}^2$, $\tau_w = \bar{\mu}_w (\partial U / \partial \eta)|_w$) approaching to the turbulent correlation implies the occurrence of a second heating peak. However, the first heating peak may extend for a longer distance along $\varphi = 0$ near a time-averaged hot streak than along other positions, resulting in a less obvious second peak induced by the transition.

To clarify mechanisms of HS and HT, a heating decomposition is conducted using DNS [27]. The heat generation rate per unit volume is related to the rate of stress work [54–56]:

$$w_{\text{all}} = \mathbf{P} : \mathbf{S} = w_{p\theta} + w_{\text{vis},\theta} + w_{\omega} + \text{B. I.}, \quad (3)$$

$$w_{p\theta} = -p\theta, \quad (4)$$

$$w_{\text{vis},\theta} = \left(\mu_b + \frac{4}{3}\mu\right)\theta^2, \quad (5)$$

$$w_{\omega} = \mu\omega^2. \quad (6)$$

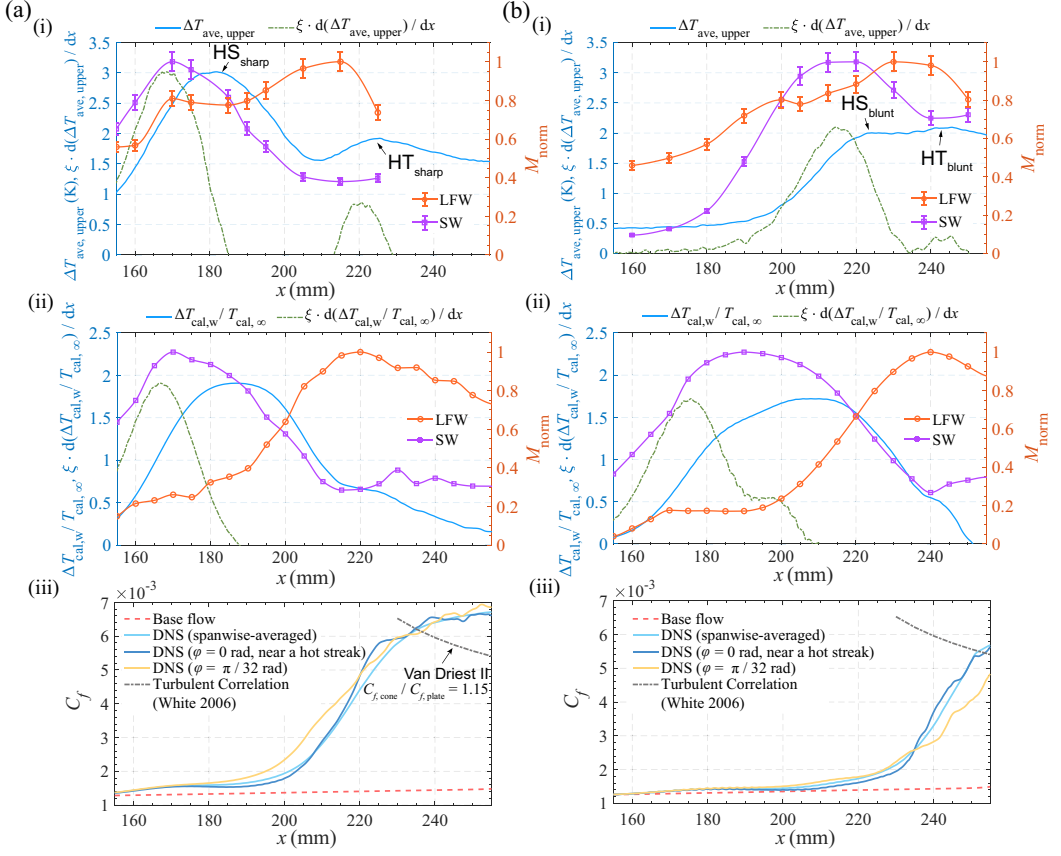


FIG. 5. Development of normalized amplitudes of instability waves (SW, second-mode waves, LFW, low-frequency waves) (the right axis), along with the variation of temperature rise and its streamwise gradient (the left axis) on (a) the sharp cone and (b) the blunt cone: (i) FLDI results; (ii) DNS results along $\phi = 0$ rad. The wave amplitude is normalized by its streamwise maximum. The temperature gradients are scaled by ξ to make its maximum equal to that of $\Delta T_{ave, upper}$ and $\Delta T_{cal, w} / T_{cal, \infty}$. (iii) the variation of skin friction coefficient C_f along different spanwise positions. The Van Driest II formula is used to provide turbulent correlation [53]. $Re_{\infty} = 10.0 \times 10^6 \text{ m}^{-1}$.

Here, \mathbf{P} is the stress tensor, $\mathbf{S} = [\nabla \mathbf{u} + (\nabla \mathbf{u})^T] / 2$ is the strain-rate tensor, and $\theta = \nabla \cdot \mathbf{u}$ is the dilatation, where \mathbf{u} is the velocity vector, $B. I.$ is a boundary integral, p is the pressure, μ_b is the bulk viscosity, μ is the dynamic viscosity, and $\omega \equiv |\boldsymbol{\omega}|$ is the vorticity magnitude. Physically, $w_{p\theta}$ and $w_{vis, \theta}$ are respectively the pressure work and the viscous dissipation when the dilatation is taken into consideration, and w_{ω} is the shear-induced viscous dissipation. The cycle-averaged pressure dilatation can be calculated as the integral

$$\langle w_{p\theta} \rangle = \frac{1}{Nt^*} \int_{t_0^*}^{t_0^* + Nt^*} [-p(t)\theta(t)] dt, \quad (7)$$

and similar integrals for the terms $\langle w_{vis, \theta} \rangle$ and $\langle w_{\omega} \rangle$ can be calculated, the sum of which gives the cycle-averaged total work as

$$\langle w_{all} \rangle = \langle w_{p\theta} \rangle + \langle w_{vis, \theta} \rangle + \langle w_{\omega} \rangle. \quad (8)$$

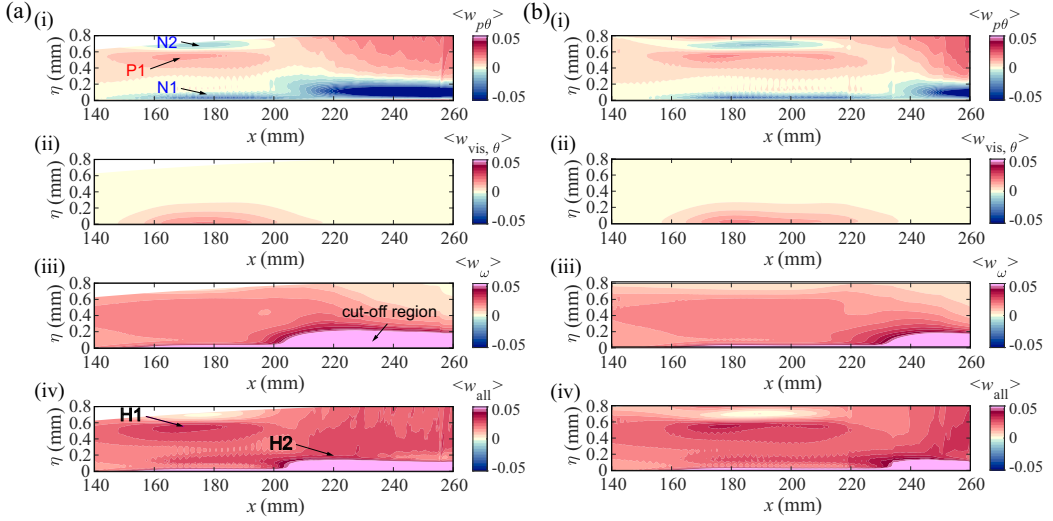


FIG. 6. Distributions of spanwise and cycle-averaged work in the boundary layer on (a) the sharp cone and (b) the blunt cone: (i) $w_{p\theta}$; (ii) $w_{vis,\theta}$; (iii) w_ω ; (iv) w_{all} . The unit of work is $\text{kg} \cdot \text{m}^{-1} \cdot \text{s}^{-3}$. All the dimensional magnitudes have been multiplied by 10^{-9} . The values in cut-off regions with pink are beyond 0.05. $\text{Re}_\infty = 10.0 \times 10^6 \text{ m}^{-1}$.

Here, t_0^* is the start time, and N , t^* are the cycle number and period of second-mode wave. The terms for grid points below $\eta = 0.8 \text{ mm}$ are integrated from the time series of calculated properties (p , \mathbf{u} , T) obtained by 1201 snapshots of the instantaneous flow field at intervals of $0.234 \mu\text{s}$. The total integral time was 0.28 ms , and $N \approx 117$ with the period $t^* \approx 2.4 \mu\text{s}$. The evaluation $\mu_b = 2\mu/3$ for nitrogen gas at 430 K was used. It would take more cycles for $\langle w_{p\theta} \rangle$ to reach a steady value in the random forcing than that in the steady forcing [57].

Figure 6 show distributions of cycle-averaged work based on spanwise-averaged DNS. The characteristics are similar for two cones. For the sharp cone, a positive region of $\langle w_{p\theta} \rangle$ denoted as P1 is located between two negative bands (N1 and N2) centered at $\eta = 0.025$ and 0.75 mm in the range of highly amplified second mode. $\langle w_{vis,\theta} \rangle$ also becomes positive below $\eta = 0.20 \text{ mm}$ in that range. Besides, $\langle w_\omega \rangle$ exhibits a broad high-value region toward $\eta = 0.20 \text{ mm}$ downstream, indicating the growing shear-induced heating. For the total work $\langle w_{all} \rangle$, two prominent regions exist. The first H1 is an olivelike band between $\eta = 0.40$ and 0.60 mm , and the second H2 is an elongated band with upper cell-like regions below $\eta = 0.45 \text{ mm}$. The two regions correspond to the saturation locations of the second mode and the low-frequency waves in Fig. 5(ii), and match the two heating peaks on the surface.

For the blunt cone, the positive regions of $\langle w_{p\theta} \rangle$ and $\langle w_{vis,\theta} \rangle$ move downstream due to the delayed saturation of the second mode. Besides, the backward location at which the broadening of $\langle w_\omega \rangle$ begins agrees with the downstream shift of the transition onset based on C_f plots. It confirms that the heating before the transition is closely related to $\langle w_{p\theta} \rangle$ and $\langle w_{vis,\theta} \rangle$ brought by the second mode, and the heating during the transition is dominated by shear-related work $\langle w_\omega \rangle$. Note that the distribution of work is not directly linked with the measured or calculated surface temperature rise. The transfer of energy from the sonic line to the wall driven by the acousticlike second mode may take effect during this process [58].

Conclusion. This study replicates experimentally that hypersonic cones can experience severe heating peaks prior to transition. It confirms that the initial peak is due to the second mode, and a small nose bluntness can only delay the evolution of the second mode, which weakens but does not eliminate the related heating. The approach of the saturation location of the second mode and the

onset location of transition indicated by the broadening disturbance spectrum leads to shorter hot streaks and low-temperature valleys, which explains the overlap observed over the blunt cone. The DNS using the random forcing replicate the measured instability evolution qualitatively, and provide further evidence for the additional aerodynamic heating induced by the second mode through a heating decomposition.

Acknowledgments. This research was supported by the National Natural Science Foundation of China under Grants No. 109103010062, No. 12072002, No. 10921202, No. 11372009, and No. 11632002, and the National Key Project GJXM92579. The authors are very grateful to Prof. Xinliang Li (LHD, Institute of Mechanics, Chinese Academy of Science) for his generosity of providing the 3D OpenCFD software.

-
- [1] J. J. Bertin and R. M. Cummings, Critical hypersonic aerothermodynamic phenomena, *Annu. Rev. Fluid Mech.* **38**, 129 (2006).
 - [2] C. R. Smith, Aerodynamic heating in hypersonic flows, *Phys. Today* **74**(11), 66 (2021).
 - [3] C. Lee and S. Chen, Recent progress in the study of transition in the hypersonic boundary layer, *Natl. Sci. Rev.* **6**, 155 (2019).
 - [4] K. Stetson, E. Thompson, J. Donaldson, and L. Siler, Laminar boundary layer stability experiments on a cone at Mach 8. Part 1: Sharp cone, in *Proceedings of the 16th Fluid and Plasmadynamics Conference* (AIAA, Danvers, MA, 1983), p. 1761.
 - [5] K. Stetson, E. Thompson, J. Donaldson, and L. Siler, Laminar boundary layer stability experiments on a cone at Mach 8. Part 2: Blunt cone, in *Proceedings of the 22nd Aerospace Sciences Meeting* (AIAA, Reno, NV, 1984), p. 0006.
 - [6] K. Stetson and R. Kimmel, On hypersonic boundary-layer stability, in *Proceedings of the 30th Aerospace Sciences Meeting and Exhibit* (AIAA, Reno, NV, 1992), p. 0737.
 - [7] J. Cleary, Effects of angle of attack and nose bluntness on the hypersonic flowover cones, in *Proceedings of the 3rd and 4th Aerospace Sciences Meeting* (AIAA, New York, NY, 1966), p. 414.
 - [8] X. Zhong, Receptivity of Mach 6 flow over a flared cone to freestream disturbance, in *Proceedings of the 42nd AIAA Aerospace Sciences Meeting and Exhibit* (AIAA, Reno, Nevada, 2004), p. 253.
 - [9] Y. Ma and X. Zhong, Receptivity of a supersonic boundary layer over a flat plate. Part 3. Effects of different types of free-stream disturbances, *J. Fluid Mech.* **532**, 63 (2005).
 - [10] K. Kara, P. Balakumar, and O. A. Kandil, Effects of nose bluntness on hypersonic boundary-layer receptivity and stability over cones, *AIAA J.* **49**, 2593 (2011).
 - [11] P. Balakumar and M. A. Kegerise, Receptivity of hypersonic boundary layers over straight and flared cones, *AIAA J.* **53**, 2097 (2015).
 - [12] M. Malik, R. Spall, and C.-L. Chang, Effect of nose bluntness on boundary layer stability and transition, in *Proceedings of the 28th Aerospace Sciences Meeting* (AIAA, Reno, NV, 1990), p. 0112.
 - [13] I. Rosenboom, S. Hein, and U. Dallmann, Influence of nose bluntness on boundary-layer instabilities in hypersonic cone flows, in *Proceedings of the 30th Fluid Dynamics Conference* (AIAA, Norfolk, VA, 1999), p. 3591.
 - [14] J. Lei and X. Zhong, Linear stability analysis of nose bluntness effects on hypersonic boundary layer transition, *J. Spacecr. Rockets* **49**, 24 (2012).
 - [15] P. Balakumar and A. Chou, Transition prediction in hypersonic boundary layers using receptivity and freestream spectra, *AIAA J.* **56**, 193 (2018).
 - [16] X. Zhong and X. Wang, Direct numerical simulation on the receptivity, instability, and transition of hypersonic boundary layers, *Annu. Rev. Fluid Mech.* **44**, 527 (2012).
 - [17] M. W. Tufts and R. L. Kimmel, Analysis of windward side hypersonic boundary layer transition on blunted cones at angle of attack, in *Proceedings of the 55th AIAA Aerospace Sciences Meeting* (AIAA, Grapevine, Texas, 2017), p. 0764.

- [18] G. H. Rushton and K. F. Stetson, Shock tunnel investigation of boundary-layer transition at M equals 5.5., *AIAA J.* **5**, 899 (1967).
- [19] E. J. Softley, Transition of the hypersonic boundary layer on a cone: part II - experiments at $M = 10$ and more on blunt cone transition, *Tech. Rep. R68SD14, General Electric Co.* (1968).
- [20] A. V. Vaganov, A. Y. Noev, V. M. Kashin, and D. V. Grachikov, Scenarios of laminar-turbulent transition reversal on blunt cone in hypersonic flow, *AIP Conf. Proc.* **2027**, 030111 (2018).
- [21] P. Paredes, M. M. Choudhari, F. Li, J. S. Jewell, R. L. Kimmel, E. C. Marineau, and G. Grossir, Nose-tip bluntness effects on transition at hypersonic speeds, *J. Spacecr. Rockets* **56**, 369 (2019).
- [22] P. Paredes, M. M. Choudhari, and F. Li, Mechanism for frustum transition over blunt cones at hypersonic speeds, *J. Fluid Mech.* **894**, A22 (2020).
- [23] D. Berridge, A. Chou, C. Ward, L. Steen, P. Gilbert, T. Juliano, S. Schneider, and J. Gronvall, Hypersonic boundary-layer transition experiments in a Mach-6 quiet tunnel, in *Proceedings of the 48th AIAA Aerospace Sciences Meeting Including the New Horizons Forum and Aerospace Exposition* (AIAA, Orlando, Florida, 2010), p. 1061.
- [24] K. J. Franko and S. K. Lele, Breakdown mechanisms and heat transfer overshoot in hypersonic zero pressure gradient boundary layers, *J. Fluid Mech.* **730**, 491 (2013).
- [25] B. C. Chynoweth, C. A. C. Ward, R. O. Henderson, C. G. Moraru, R. T. Greenwood, A. D. Abney, and S. P. Schneider, Transition and instability measurements in a Mach 6 quiet wind tunnel, in *Proceedings of the 52nd Aerospace Sciences Meeting* (AIAA, National Harbor, Maryland, 2014), p. 0074.
- [26] Y. Zhu, X. Chen, J. Wu, S. Chen, C. Lee, and M. Gad-el Hak, Aerodynamic heating in transitional hypersonic boundary layers: Role of second-mode instability, *Phys. Fluids* **30**, 011701 (2018).
- [27] Y. Zhu, C. Lee, X. Chen, J. Wu, S. Chen, and M. Gad-el Hak, Newly identified principle for aerodynamic heating in hypersonic flows, *J. Fluid Mech.* **855**, 152 (2018).
- [28] C. Zhang, Q. Tang, and C.-B. Lee, Hypersonic boundary-layer transition on a flared cone, *Acta Mech. Sin.* **29**, 48 (2013).
- [29] W. Zhu, D. Gu, W. Si, M. Zhang, S. Chen, C. Smith, Y. Zhu, and C. Lee, Instability evolution in the hypersonic boundary layer over a wavy wall, *J. Fluid Mech.* **943**, A16 (2022).
- [30] S. P. Schneider, Developing mechanism-based methods for estimating hypersonic boundary-layer transition in flight: The role of quiet tunnels, *Prog. Aerosp. Sci.*, **72**, 17 (2015).
- [31] D. Xu, P. Ricco, and L. Duan, Görtler instability and transition in compressible flows, *AIAA J.* **62**, 489 (2024).
- [32] Y. Zhu, C. Zhang, X. Chen, H. Yuan, J. Wu, S. Chen, C. Lee, and M. Gad-el Hak, Transition in hypersonic boundary layers: Role of dilatational waves, *AIAA J.* **54**, 3039 (2016).
- [33] C. Zhang, Y. Zhu, X. Chen, H. Yuan, J. Wu, S. Chen, C. Lee, and M. Gad-el Hak, Transition in hypersonic boundary layers, *AIP Adv.* **5**, 107137 (2015).
- [34] B. C. Chynoweth, A New roughness array for controlling the nonlinear breakdown of secondmode waves at Mach 6, Master's thesis, Purdue University, 2015.
- [35] W. Si, G. Huang, Y. Zhu, S. Chen, and C. Lee, Hypersonic aerodynamic heating over a flared cone with wavy wall, *Phys. Fluids* **31**, 051702 (2019).
- [36] N. J. Parziale, J. E. Shepherd, and H. G. Hornung, Free-stream density perturbations in a reflected-shock tunnel, *Exp. Fluids* **55**, 1665 (2014).
- [37] Y. Xiong, T. Yu, L. Lin, J. Zhao, and J. Wu, Nonlinear instability characterization of hypersonic laminar boundary layer, *AIAA J.* **58**, 5254 (2020).
- [38] P. Welch, The use of fast Fourier transform for the estimation of power spectra: A method based on time averaging over short, modified periodograms, *IEEE Trans. Audio Electroacoust.* **15**, 70 (1967).
- [39] X. Li, D. Fu, and Y. Ma, Direct numerical simulation of hypersonic boundary layer transition over a blunt cone, *AIAA J.* **46**, 2899 (2008).
- [40] W. Ba, M. Niu, and C. Su, Hypersonic boundary-layer receptivity over circular cones with ellipsoidal/spherical noses, *AIAA J.* **61**, 1 (2022).
- [41] C. Hader and H. F. Fasel, Towards simulating natural transition in hypersonic boundary layers via random inflow disturbances, *J. Fluid Mech.* **847**, R3 (2018).

- [42] See Supplemental Material at <http://link.aps.org/supplemental/10.1103/PhysRevFluids.9.L071901> for the details of the present DNS setup, which includes Refs. [43–47].
- [43] X. Li, D. Fu, and Y. Ma, Direct numerical simulation of hypersonic boundary layer transition over a blunt cone with a small angle of attack, *Phys. Fluids* **22**, 025105 (2010).
- [44] X. Chen, G. L. Huang, and C. B. Lee, Hypersonic boundary layer transition on a concave wall: Stationary Görtler vortices, *J. Fluid Mech.* **865**, 1 (2019).
- [45] X. Zhong and Y. Ma, Boundary-layer receptivity of mach 7.99 flow over a blunt cone to free-stream acoustic waves, *J. Fluid Mech.* **556**, 55 (2006).
- [46] R. L. Kimmel, M. A. Klein, and S. N. Schwoerke, Three-dimensional hypersonic laminar boundary-layer computations for transition experiment design, *J. Spacecr. Rockets* **34**, 409 (1997).
- [47] B. Wan, J. Luo, and C. Su, Response of a hypersonic blunt cone boundary layer to slow acoustic waves with assessment of various routes of receptivity, *Appl. Math. Mech.-Engl. Ed.* **39**, 1643 (2018).
- [48] A. Chou, C. Ward, L. Letterman, S. Schneider, R. Luersen, and M. Borg, Transition research with temperature-sensitive paints in the Boeing/AFOSR Mach-6 quiet tunnel, in *Proceedings of the 41st AIAA Fluid Dynamics Conference and Exhibit* (AIAA, Honolulu, Hawaii, 2011), p. 3872.
- [49] J. Sivasubramanian and H. F. Fasel, Direct numerical simulation of transition in a sharp cone boundary layer at Mach 6: Fundamental breakdown, *J. Fluid Mech.* **768**, 175 (2015).
- [50] W. Zhu, D. Gu, W. Si, S. Chen, Y. Zhu, and C. Lee, Reduced aerodynamic heating in a hypersonic boundary layer by a wavy wall, *Sci. Bull.* **67**, 988 (2022).
- [51] C. Lee and J.-Z. Wu, Transition in wall-bounded flows, *Appl. Mech. Rev.* **61**, 030802 (2008).
- [52] X. Chen, Y. Zhu, and C. Lee, Interactions between second mode and low-frequency waves in a hypersonic boundary layer, *J. Fluid Mech.* **820**, 693 (2017).
- [53] F. M. White, *Viscous Fluid Flow* (McGraw-Hill, 2006), pp. 599–561.
- [54] S. K. Lele, Compressibility effects on turbulence, *Annu. Rev. Fluid Mech.* **26**, 211 (1994).
- [55] J.-Z. Wu, Y. Zhou, and M. Fan, A note on kinetic energy, dissipation and enstrophy, *Phys. Fluids* **11**, 503 (1999).
- [56] J.-Z. Wu, H.-Y. Ma, and M.-D. Zhou, *Vorticity and Vortex Dynamics* (Springer, 2006), pp. 54–55.
- [57] Y. Zhu, D. Gu, W. Zhu, S. Chen, C. Lee, and E. S. Oran, Dilatational-wave-induced aerodynamic cooling in transitional hypersonic boundary layers, *J. Fluid Mech.* **911**, A36 (2021).
- [58] J. Yu, Y. Zhu, D. Gu, and C. Lee, A thermoacoustic heat pump driven by acoustic waves in a hypersonic boundary layer, *Phys. Fluids* **34**, 011703 (2022).